ELSEVIER

Available online at www.sciencedirect.com

ScienceDirect

Journal of Catalysis 246 (2007) 370–381

JOURNAL OF CATALYSIS

www.elsevier.com/locate/jcat

Molecular/electronic structure–surface acidity relationships of model-supported tungsten oxide catalysts

Taejin Kim [a], Andrew Burrows [b], Christopher J. Kiely [b], Israel E. Wachs [a,*]

[a] *Operando Molecular Spectroscopy & Catalysis Laboratory, Chemical Engineering Department, Lehigh University, Bethlehem, PA 18015, USA*
[b] *Center for Advanced Materials and Nanotechnology, Materials Science & Engineering Department, Lehigh University, Bethlehem, PA 18015, USA*

Received 30 August 2006; revised 20 October 2006; accepted 30 December 2006

Abstract

A series of model-supported WO_3 catalysts were synthesized on preformed Al_2O_3, Nb_2O_5, TiO_2, and ZrO_2 supports by impregnation of aqueous ammonium metatungstate, $(NH_4)_{10}W_{12}O_{41}\cdot 5H_2O$. The molecular and electronic structures of the supported tungsten oxide phases were determined with in situ Raman and UV–vis spectroscopy, respectively. The supported tungsten oxide structures are the same on all oxide supports as a function of tungsten oxide surface density (W/nm^2). Below monolayer coverage (<5 W/nm^2), both monotungstate and polytungstate surface WO_x species are present under dehydrated conditions and the polytungstate/monotungstate ratio increases with increasing surface coverage. Above monolayer coverage (>5 W/nm^2), crystalline WO_3 nanoparticles are present on top of the surface WO_x monolayer. Above ∼10 W/nm^2, bulk-like WO_3 crystallites become dominant. The number of catalytic active sites and surface chemistry of the supported tungsten oxide phases were chemically probed with CH_3OH dehydration to CH_3OCH_3. The specific oxide support was found to significantly affect the relative catalytic acidity of the surface WO_x species ($Al_2O_3 \gg TiO_2 > Nb_2O_5 > ZrO_2$) to that of the supported WO_3 nanoparticles. Consequently, no general relationship exists between the molecular/electronic structures or domain size and the specific catalytic acidity of the supported tungsten oxide phases present in the model-supported WO_3 catalysts.

Keywords: Spectroscopy; Raman; UV–vis; TPSR; HR-TEM; Catalysts; Supported; WO_3; Al_2O_3; ZrO_2; TiO_2; Nb_2O_5; CH_3OH; CH_3OCH_3; Dehydration

1. Introduction

Supported tungsten oxide catalysts are used in many significant industrial applications and are known to be efficient solid acid catalysts [1,2]. Tungsten oxide on alumina catalysts are used for hydrotreating and for hydrocarbon cracking reactions [3–7], and also exhibit enhanced resistance to reduction [8]. Tungsten oxide supported on titania, in combination with vanadia, is effective for both the selective catalytic reduction of NO by NH_3 to N_2/H_2O and for alkene isomerization [9,10]. As an alternative to the sulfated zirconia solid acid catalyst, supported WO_3/ZrO_2 catalysts also have been reported to be active for the isomerization of C_4–C_8 alkanes [11–13]. In contrast to the above supported tungsten oxide catalytic systems, the supported WO_3/Nb_2O_5 catalysts have not received as much attention [14–16].

In many cases, the interaction of a catalytic active component, such as tungsten oxide, with an oxide support (Al_2O_3, ZrO_2, TiO_2, and Nb_2O_5) can dramatically alter the structural and catalytic properties of supported catalytic active component [17]. For most such strongly interacting oxide systems, the supported catalytic active metal oxide phase is molecularly dispersed as a two-dimensional metal oxide overlayer on a high surface area support oxide [17]. The nature of the surface tungsten oxide phases on oxide supports have been characterized with many different techniques to provide insights into their molecular and electronic structures as well as provide information their corresponding surface chemical properties [17–27]. In spite of the large body of literature on this subject, the molecular/electronic structure–catalytic activity relationships of supported tungsten oxide catalysts are still not satisfactorily understood. Consequently, the objective of this paper is to investigate

---

[*] Corresponding author. Fax: +1 610 758 6555.
E-mail address: iew0@lehigh.edu (I.E. Wachs).

0021-9517/$ – see front matter © 2007 Elsevier Inc. All rights reserved.
doi:10.1016/j.jcat.2006.12.018

the molecular/electronic and the surface reactivity properties of model-supported tungsten oxide catalysts and to establish the relationships between these parameters. In the present study both the surface tungsten oxide coverage (W/nm^2) and the specific oxide support, preformed model supports, were varied over a wide range to carefully examine the influence of these two significant parameters. The tungsten oxide molecular structures were determined with in situ Raman spectroscopy and the corresponding electronic structures were determined with in situ UV–vis diffuse reflectance spectroscopy (DRS). The acidic nature of the supported tungsten oxide phases were chemically probed with temperature programmed surface reaction (TPSR) spectroscopy and steady-state dehydration of methanol to dimethyl ether (CH_3OCH_3).

2. Experimental

2.1. Catalyst synthesis

The supported tungsten oxide catalysts were all prepared by incipient wetness impregnation of aqueous ammonium metatungstate, $(NH_4)_{10}W_{12}O_{41}\cdot 5H_2O$ (Pfaltz & Bauer, 99.5% purity), onto different oxide supports: Al_2O_3 (Harshaw/Engelhard, 178 m^2/g), TiO_2 (Degussa P-25, 51 m^2/g), Nb_2O_5 (CBMM AD1927 HY-340, 66 m^2/g), and ZrO_2 (Degussa, 60 m^2/g). After impregnation, the samples were initially dried at room temperature overnight and then calcined in flowing air for 4 h at 450 °C. Several supported WO_3/ZrO_2 catalysts were also calcined at elevated temperatures (700–900 °C) to examine the effect of calcination temperature.

2.2. BET specific surface area measurement

The BET surface areas of the samples were measured by nitrogen adsorption–desorption in flowing N_2 at −196 °C with a Quantasorb surface area analyzer (Quantachrome Corporation, Model OS-9). A sample quantity of ~0.3 g was used for the measurement, and the sample was outgassed at 250 °C before N_2 adsorption (Quantachrome Corporation, Model QT-3).

2.3. Raman spectroscopy

The Raman spectra of the dehydrated supported tungsten oxide catalysts were obtained with either visible (532 nm) or UV (325 nm) excitation (Horiba-Jobin Yvon LabRam-HR). The UV laser excitation was generated from a He–Cd laser (Kimmon, Model IK5751 I-G, 30 mW) and the visible excitation was generated by a Yag double-diode pumped laser (coherent 315 m, 20 mW). The scattered photons were directed into a single monochromator and focused onto a LN_2 cooled CCD detector (JY-CCD3000V). The Raman spectrometer was equipped with an in situ environmental cell (Linkam T1500 cell) where both the temperature and the gaseous composition were controllable. The catalysts were maintained in loose powder form, initially dehydrated at 450 °C for 1 h in flowing 10% O_2/He (Airgas, ultra-high purity and hydrocarbon-free), and the Raman spectra of the dehydrated samples were collected after cooling the catalysts back to room temperature in the flowing 10% O_2/He gas. The spectral acquisition time used was 30 scans of 30 s/scan for a total of 15 min/spectrum.

2.4. UV–vis diffuse reflectance spectroscopy (DRS)

The UV–vis spectra of the dehydrated supported tungsten oxide catalysts were measured with a Varian Cary 5E UV–vis–NIR spectrophotometer. The catalysts in powder form were loaded into an environmental cell (Harrick, HVC-DR2) for obtaining their UV–vis spectra. The UV–vis spectra of the dehydrated samples were obtained at room temperature after calcination at 400 °C in flowing 10% O_2/He gas for 1 h and cooling back to room temperature. A magnesium oxide sample was used as the standard for obtaining the baseline. Microsoft Excel software was used to calculate the Kubelka–Munk function $F(R\infty)$ and the edge energy (Eg) from the absorbance data. Below 300 nm, the absorbance signal was unacceptably noisy and a filter (Varian, 1.5 ABS) was used to minimize the background noise. The UV–vis spectra were only collected for the supported WO_3/ZrO_2 and WO_3/Al_2O_3 catalysts because the strong oxide absorbance by the TiO_2 and Nb_2O_5 supports in the region of interest prevented collection of their supported tungsten oxide UV–vis spectra. The Al_2O_3 support possesses no absorbance and the ZrO_2 support exhibits very weak absorbance in the region of interest. The supported WO_3/ZrO_2 UV–vis spectra were background subtracted with the ZrO_2 support spectrum to account for zirconia's weak contribution to the UV–vis spectrum. In addition, the Eg values for the 2D surface WO_x and the 3D WO_3 phases were independently determined by background subtracting the 2D surface WO_x monolayer UV–vis DRS contribution when monolayer surface coverage was exceeded.

2.5. High resolution-transmission electron microscopy (HR-TEM)

Samples for HR-TEM examination were prepared by dispersing the catalyst powder in high purity ethanol, then allowing a drop of the suspension to evaporate on a holey carbon film supported by a 300 mesh copper TEM grid. HR-TEM images of the ambient samples were obtained using a JEOL 2200FS transmission electron microscope, having an accelerating voltage of 200 kV, a point-to-point resolution of 0.19 nm and an information limit of 0.11 nm. Fourier transform (FT) analyses of lattices fringe periodicities and inter-planar angles were carried out using digital micrograph.

2.6. CH_3OH temperature-programmed surface reaction (TPSR) spectroscopy

Methanol TPSR spectroscopy was performed on an Altamira temperature programmed system (AMI-200) equipped with an online quadrupole mass spectrometer (Dycor Dymaxion DME200MS). Samples of ~100 mg were loaded into a U-shaped quartz tube and initially calcined at 400 °C (Airgas, ultra zero grade air, 30 ml/min) for 40 min to remove any possible adsorbed organic impurities and to dehydrate the catalysts. To ensure that the supported tungsten oxide species on the catalysts remain in a fully oxidized state, the pretreated samples were first cooled down in flowing air to 110 °C and then the gas stream was switched to an ultra high purity He (Airgas) flow on further cooling to 100 °C. After flushing with flowing He for another 30 min at 100 °C to remove any physically adsorbed oxygen and possible background gases, a CH_3OH/He gas mixture feed (30 ml/min) containing 2000 ppm methanol was introduced for chemisorption for 30 min. Previous work demonstrated that methanol adsorption at 100 °C minimizes the formation of physically adsorbed methanol on the samples because physically adsorbed CH_3OH desorbs below this temperature from oxide surfaces [28,29]. After methanol adsorption, the samples were again purged at 100 °C with flowing He for an additional hour to remove any residual physically adsorbed methanol. The CH_3OH-TPSR experiments were performed with a heating rate of 10 °C/min in flowing UHP He and the desorbing molecules were monitored with the online MS. The m/e values used to detect the different desorption products were CH_3OH ($m/e = 31$), H_2CO ($m/e = 30$), CH_3OCH_3 (DME; $m/e = 45$), $(CH_3O)_2CH_2$ (DMM; $m/e = 75$), H_2O ($m/e = 18$), CO_2 ($m/e = 44$), and CO ($m/e = 28$). For those desorbing molecules that gave rise to several fragments in the mass spectrometer, additional m/e values were also collected to further confirm their identity. The activation energy for formation of dimethyl ether was calculated using the Redhead equation for first-order kinetics [30]. Previous studies demonstrated that the rate-determining step in methanol dehydration involves the first-order process that breaks the C–O bond in the surface CH_3O^* intermediate [31]. In addition, the area under the DME/CH_3OH-TPSR curve corresponds to the number of exposed surface acid sites.

2.7. Steady-state dehydration of methanol to dimethyl ether

Methanol dehydration was used to chemically probe the catalytic activity and product selectivity of the supported tungsten oxide catalysts. The dehydration of methanol was examined in a fixed-bed reactor at 230 °C with 30 mg of catalyst. The catalysts were suspended between two layers of quartz wool in a vertical glass tube. The volume composition of the gaseous reactant feed was $CH_3OH/O_2/He = 6/13/81$ (mol%) with a total flow rate of 100 ml/min from the top to the bottom of the reactor. The outlet of the reactor to the gas chromatograph was heated at ∼130 °C in order to avoid product condensation. Online analysis of the methanol conversions and reaction products was performed with an HP-5840A gas chromatograph containing two packed columns (Porapack R and Carbosieve SII) and two detectors (TCD and FID). Blank runs without the catalysts demonstrated negligible methanol conversion in the reactor system. The supported tungsten oxide catalysts were pretreated at 350 °C for 30 min in a stream of O_2/He before each run. The catalytic experiments were run for 4 h at 230 °C to obtain the methanol conversion, selectivity, and activity. The steady-state methanol dehydration catalytic data were expressed in terms of turnover frequency (TOF: number of DME molecules/surface acid site/s). For the supported tungsten oxide catalysts below monolayer surface coverage, the number of surface acid sites was taken as the number of surface WO_x species, which assumed 100% dispersion and was independently confirmed with Raman spectroscopy. Above monolayer surface tungsten oxide coverage, the number of exposed surface acid sites was determined by the area under the DME/CH_3OH-TPSR curves and normalized to the value for monolayer coverage.

3. Results

3.1. BET specific surface area and tungsten oxide surface density

The BET surface area and tungsten oxide surface density (W/nm^2) for the supported tungsten oxide catalysts were determined and are listed in Table 1. The BET surface area continuously decreases with increasing tungsten oxide loading due to the additional mass introduced by the supported tungsten oxide phase. The tungsten oxide surface density (W/nm^2) was calculated by using the initial BET surface area of the oxide supports because the supports retain their initial BET values for this rather mild calcination temperature and in the presence of surface tungsten oxide species that are known to retard sintering of oxide support.

3.2. In situ Raman spectroscopy

3.2.1. Supported WO_3/Al_2O_3 catalysts

The UV Raman spectra of the dehydrated WO_3/Al_2O_3 samples as a function of surface tungsten oxide density are presented in Fig. 1. The UV excitation was used because of sample fluorescence when excited in the visible region [32]. At low surface tungsten oxide density (0.5–4 W/nm^2), only the Raman band characteristic of dehydrated surface WO_x species is present. The surface nature of these dehydrated tungsten oxide species is confirmed by their reversible structural transformations on hydration–dehydration treatments (not shown for brevity). The Raman band in the 1003–1015 cm^{-1} region arises

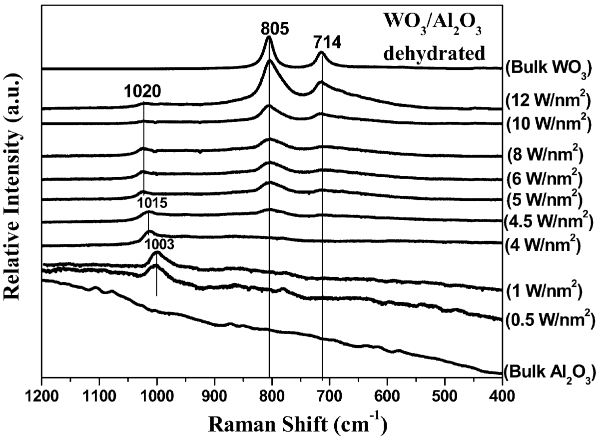

Fig. 1. UV Raman spectra of the model-supported WO_3/Al_2O_3 catalysts under dehydrated conditions.

Table 1
BET surface area and tungsten oxide surface density (W/nm^2) of the supported WO_3 catalysts on the model oxide supports (TiO_2, Nb_2O_5, Al_2O_3, and ZrO_2)

Sample (calcination temperature, °C)	Surface density (W/nm^2)	BET surface area (m^2/g)
Bulk TiO_2	0.0	51.0
5.0 wt% WTi (450)	2.7	48.1
7.3 wt% WTi (450)	4.0	46.4
8.1 wt% WTi (450)	4.5	46.1
13.6 wt% WTi (450)	8.0	43.0
16.4 wt% WTi (450)	10.0	41.4
19.1 wt% WTi (450)	12.0	39.3
Bulk Nb_2O_5	0.0	66.0
3.2 wt% WNb (450)	1.3	64.0
9.2 wt% WNb (450)	4.0	56.7
10.2 wt% WNb (450)	4.5	55.8
16.9 wt% WNb (450)	8.0	51.3
20.3 wt% WNb (450)	10.0	47.8
23.4 wt% WNb (450)	12.0	43.6
Bulk Al_2O_3	0.0	178.0
3.2 wt% WAl (450)	0.5	166.2
6.4 wt% WAl (450)	1.0	166.0
21.5 wt% WAl (450)	4.0	158.8
23.5 wt% WAl (450)	4.5	145.6
25.6 wt% WAl (450)	5.0	133.0
29.1 wt% WAl (450)	6.0	126.0
35.4 wt% WAl (450)	8.0	125.3
40.7 wt% WAl (450)	10.0	108.2
45.1 wt% WAl (450)	12.0	96.9
57.8 wt% WAl (450)	20.0	75.0
Bulk ZrO_2	0.0	60.0
1 wt% WZr (450)	0.4	59.9
4 wt% WZr (450)	1.8	59.6
5 wt% WZr (450)	2.3	59.4
6 wt% WZr (450)	2.8	59.3
7 wt% WZr (450)	3.3	59.3
8.3 wt% WZr (450)	3.9	58.7
9.4 wt% WZr (450)	4.5	55.6
10 wt% WZr (450)	4.8	55.3
12 wt% WZr (450)	5.9	54.5
15 wt% WZr (450)	7.6	49.0
20 wt% WZr (450)	10.8	45.3
21.7 wt% WZr (450)	12.0	45.1
25.0 wt% WZr (450)	14.4	45.0
40.0 wt% WZr (450)	28.9	32.8

from the symmetric stretching vibrations of the terminal W=O bonds of surface WO_x species [15,33]. The shift of the surface W=O band with increasing tungsten oxide surface density is related to the polymerization of the surface WO_x species from monotungstate to polytungstate species [15]. No Raman bands due to crystalline WO_3 particles at ~805 and ~714 cm^{-1} are present for samples with less than 5 W/nm^2 [34]. At tungsten oxide surface densities of 5 W/nm^2 and above, Raman bands of crystalline WO_3 also appear at ~805 and ~714 cm^{-1} (see Fig. 1 for the bulk crystalline WO_3 Raman spectrum). Note the Raman bands for the alumina-supported WO_3 crystallites are much broader than that of the crystalline bulk WO_3, which reflects the nanoparticle (NP) dimension of the supported WO_3 crystallites. In addition, the Raman band of the terminal W=O bond of the surface WO_x species further shifts from ~1015 to ~1020 cm^{-1} with increasing surface WO_x density.

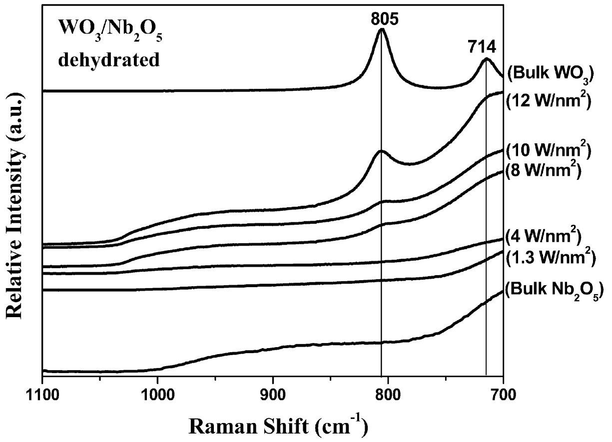

Fig. 2. Visible Raman spectra of the model-supported WO_3/Nb_2O_5 catalysts under dehydrated conditions.

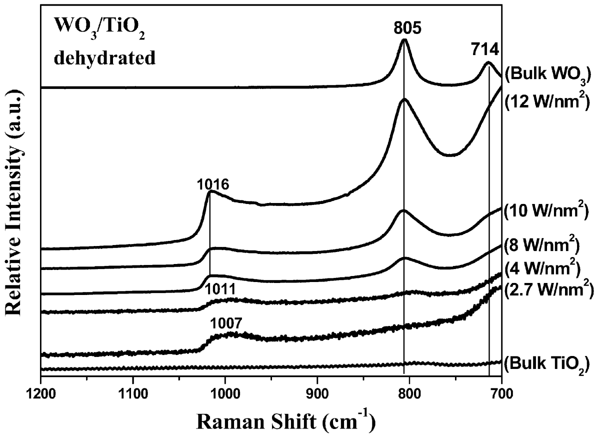

Fig. 3. Visible Raman spectra of the model-supported WO_3/TiO_2 catalysts under dehydrated conditions.

3.2.2. Supported WO_3/Nb_2O_5 catalysts

The visible Raman spectra of the dehydrated supported WO_3/Nb_2O_5 catalysts in the 1.3–12 W/nm^2 range are presented in Fig. 2. The Raman spectra are limited to above 700 cm^{-1} because of the strong Raman vibrations of the Nb_2O_5 support below 700 cm^{-1}. Crystalline WO_3 NPs are not present in the 1.3–4 W/nm^2 range and only appear at higher tungsten oxide surface density. Again, note that the supported WO_3 NPs give rise to a broader Raman band at 805 cm^{-1} than that for the corresponding bulk crystalline WO_3 at higher tungsten oxide surface density (>4 W/nm^2). The surface WO_x species give rise to a weak and broad Raman band in the 900–1000 cm^{-1} region against the Nb_2O_5 support background that are further enhanced when the Nb_2O_5 contribution is subtracted (not shown for brevity).

3.2.3. Supported WO_3/TiO_2 catalysts

The visible Raman spectra of dehydrated supported WO_3/TiO_2 catalysts are shown in Fig. 3.

The Raman spectra are limited to above 700 cm^{-1} because of the strong vibrations of the TiO_2 support at lower values. In fact, the rising background below 750 cm^{-1} is already a vi-

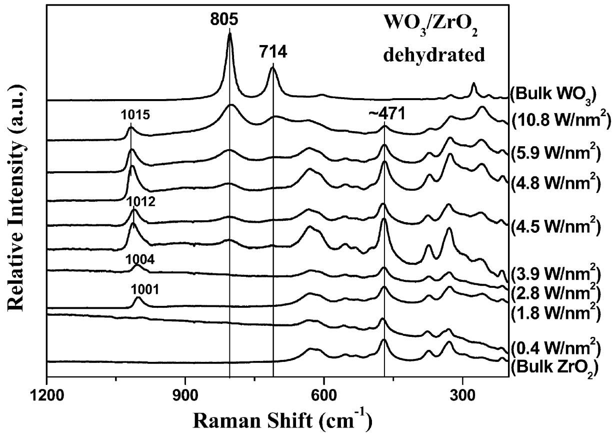

Fig. 4. Visible Raman spectra of the model-supported WO_3/ZrO_2 catalysts under dehydrated conditions.

brational contribution from the TiO_2 support. The dehydrated surface WO_x species gives rise to Raman bands in the ∼1000–1016 cm^{-1} with increasing tungsten oxide surface coverage. This vibrational shift with tungsten oxide surface coverage is related to the continuous polymerization of the surface monotungstate species to surface polytungstate species [15]. The additional Raman band at ∼805 cm^{-1} at higher surface tungsten oxide density (>4 W/nm^2) reflects the presence of crystalline WO_3 NPs.

3.2.4. Supported WO_3/ZrO_2 catalysts

The visible Raman spectra of the dehydrated supported WO_3/ZrO_2 catalysts are presented in Fig. 4. The Raman spectrum for the 0.4 W/nm^2 sample does not give rise to detectable bands for the surface WO_x species against the strong Raman spectrum of the ZrO_2 support. The Raman band of the surface WO_x species shifts from 1001 to 1015 cm^{-1} with increasing surface WO_x coverage reflecting the transformation of surface monotungstate to polytungstate species. Crystalline WO_3 NPs are present at ∼4 W/nm^2 and higher surface density with Raman bands at 805 and 714 cm^{-1}.

3.2.5. Monolayer surface WO_x coverage on oxide supports

Monolayer surface WO_x coverage for the supported WO_3/ZrO_2 catalyst system was determined by using the strong ∼471 cm^{-1} band of the ZrO_2 support as an internal standard. Two different methods were used to determine monolayer surface WO_x coverage. The first method plotted the intensity of the Raman band of the dehydrated surface WO_x species in the 1000–1020 cm^{-1} region by normalizing this band to the ZrO_2 internal standard as a function of tungsten oxide surface density. The normalized Raman intensity of the dehydrated surface WO_x species as a function of the tungsten oxide surface density on the ZrO_2 support is presented in Fig. 5a. The normalized Raman intensity for the surface WO_x species linearly increases with W/nm^2 and levels off at ∼4.5 W/nm^2. Note that no further increase in the normalized surface WO_x Raman intensity occurs above ∼4.5 W/nm^2, which reflects saturation of monolayer surface coverage of the surface WO_x species on ZrO_2. The second method plotted the normalized Raman intensity of the crystalline WO_3 NPs (∼805 cm^{-1}) as a function of tungsten oxide surface density and is shown in Fig. 5b. The normalized crystalline WO_3 NP Raman intensity is zero until ∼4 W/nm^2 and then increases linearly with surface W density. Extrapolating the linear portion of the curve back to its intercept with the x-axis gives a value of ∼4.5 W/nm^2. This extrapolation method avoids considering the formation of small amounts of WO_3 NPs that typically form as monolayer surface coverage is approached. Thus, both Raman methods quantitatively demonstrate that monolayer surface coverage occurs at ∼4.5 W/nm^2 for the supported WO_3/ZrO_2 catalyst system.

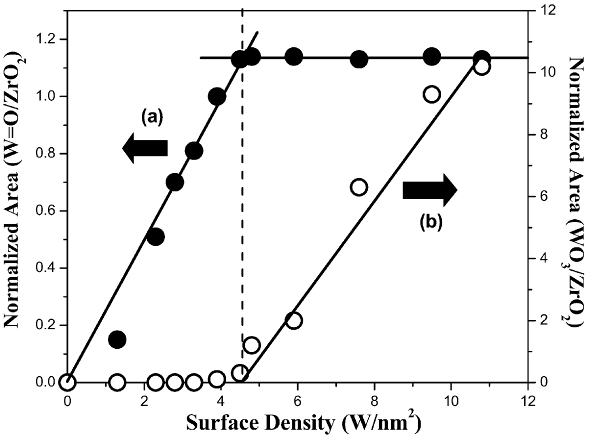

Fig. 5. Plots of normalized Raman intensity of the dehydrated surface WO_x species (∼1000–1020 cm^{-1}) and crystalline WO_3 particles (∼805 cm^{-1}) as a function of tungsten oxide surface density (W/nm^2) on the model ZrO_2 support.

Comparison of the Raman spectra of the supported WO_3/ZrO_2 catalysts with the other supported tungsten oxide catalysts also provides information about monolayer surface WO_x coverage on these other oxide supports. Crystalline WO_3 NPs are not present below ∼4 W/nm^2 on any of the supports and the intensity of the crystalline WO_3 NPs increases with increasing W/nm^2 above ∼4 W/nm^2. Furthermore, the appearance of crystalline WO_3 NPs at ∼4.5 W/nm^2 was also found to be independent of catalyst calcination temperature reflecting the universal value of ∼4.5 W/nm^2 for monolayer surface WO_x coverage on oxide supports.

3.3. In situ UV–vis diffuse reflectance spectroscopy (DRS)

The UV–vis DRS Eg values for the dehydrated supported WO_3/ZrO_2 (represented by open symbols) and WO_3/Al_2O_3 (represented by solid symbols) are presented in Fig. 6 as functions of the tungsten oxide surface density (W/nm^2) and calcination temperature. Recall that the UV–vis DRS for the supported WO_3/TiO_2 and WO_3/Nb_2O_5 were not collected because of the strong absorbance by the TiO_2 and Nb_2O_5 supports in the region of interest. Both supported tungsten oxide catalyst systems exhibit the same trend with increasing W/nm^2 and essentially fall on the same curve. In addition, the data points for the supported WO_3/ZrO_2 calcined at different temperatures also fall on the same curve. Thus, the UV–vis DRS Eg values are independent of the specific oxide support and calcination tem-

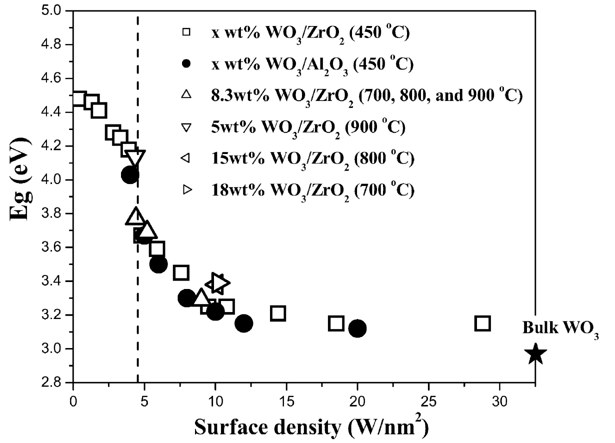

Fig. 6. Plot of UV–vis DRS Eg values for the dehydrated model-supported WO_3/ZrO_2 and WO_3/Al_2O_3 catalysts calcined at different temperatures as a function of tungsten oxide surface density (W/nm^2).

perature when plotted as a function of tungsten oxide surface density. The universal Eg vs tungsten oxide surface density plot exhibits three distinct regions: (1) modest decrease in Eg values between 0 and 4.5 W/nm^2, (2) somewhat greater decrease in Eg values between 4.5 and 10 W/nm^2, and (3) relatively constant Eg values above 10 W/nm^2 that asymptotically approach the Eg value of large bulk WO_3 crystals. The initial Eg values at the lowest surface coverage exhibit a value of ~4.5 eV that continues to decrease with increasing surface WO_x coverage up to monolayer coverage of ~4.5 W/nm^2. The initial Eg value is between the Eg values for isolated (Na_2WO_4 at ~5.2 eV) and extensively polymerized ($Na_2W_2O_7$ at 4.2 eV) WO_x structures suggesting a mixture of these two surface WO_x structures below monolayer surface coverage. Furthermore, the Eg value monotonically decreases with increasing surface W density up to monolayer coverage reflecting that the surface WO_x species are becoming more polymerized as the surface WO_x density increases in the submonolayer region. The Eg value at monolayer surface WO_x coverage corresponds to that of a linear WO_x polymer present [e.g., $(NH_4)_2W_2O_7$]. Above 4.5 W/nm^2, the Eg value continues to rapidly decrease and Raman simultaneously detects the presence of crystalline WO_3 NPs in this tungsten oxide surface density region. The Eg values of the supported WO_3 crystallites, however, are greater than that for large bulk WO_3 crystallites, because they are present as WO_3 NPs between 4.5 and 10 W/nm^2. Above 10 W/nm^2, the Eg values remain relatively constant with increasing surface W density, because the WO_3 particles are much larger in this tungsten oxide surface density region and exhibit bulk-like characteristics. In summary, UV–vis DRS in combination with Raman spectroscopy is able to discriminate between isolated surface WO_x species, polymeric surface WO_x species, WO_3 NPs and large bulk-like WO_3 particles.

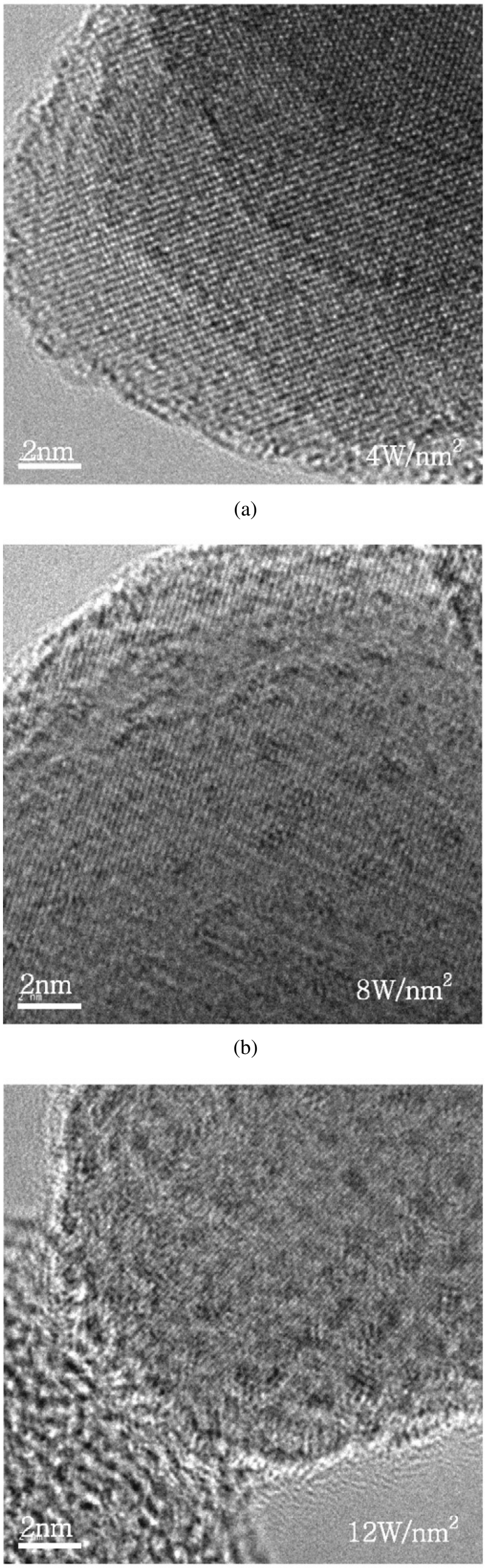

(a)

(b)

(c)

Fig. 7. HR-TEM images of (a) 4, (b) 8, and (c) 12 W/nm^2 WO_3/ZrO_2 catalysts.

3.4. High resolution-transmission electron microscopy (HR-TEM)

Representative HR-TEM images of the supported WO_3/ZrO_2 catalysts are shown in Figs. 7a–7c for the catalysts with a surface W/ZrO_2 density of 4, 8, and 12 W/nm^2, respectively. All of the HR-TEM images obtained clearly display crystalline ZrO_2 lattice fringes, especially at lower magnifications. The additional presence of an amorphous WO_x overlayer, and very

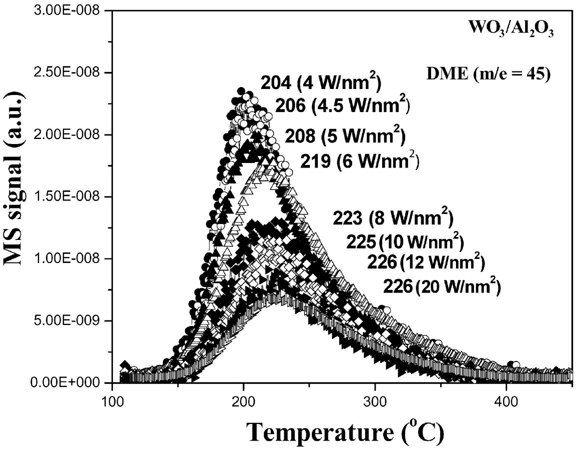

Fig. 8. CH_3OH-TPSR spectra for methanol dehydration to CH_3OCH_3 over the model supported WO_3/Al_2O_3 catalysts as a function of the tungsten oxide surface density (W/nm^2).

small tungsten oxide NPs that are around 1 nm in size are also suggested by this sequence of images. The amorphous overlayer of the surface WO_x species appears most prominently at the edges of the support particles when viewed in profile. In addition, very small NPs possessing a lateral dimension of around 1 nm can be seen as darker flecks against the ZrO_2 support, and appear by virtue of their mass contrast. A general trend of increasing number density of these dark flecks with increasing surface W/nm^2 density was observed, although it is interesting to note that their average lateral size did not increase markedly with W loading. These dark flecks are thought to arise from the presence of crystalline WO_3 nanoparticles and possibly also from hydrated $(WO_x)\cdot nH_2O$ clusters. It should, however, be noted that the WO_x overlayers on these ZrO_2 support particles are very sensitive to modification in the electron beam and great care needs to be taken to minimize the electron dose during HRTEM imaging experiments.

3.5. *CH_3OH-TPSR spectroscopy*

Methanol was used as a chemical probe molecule because it readily discriminates between surface acidic sites (formation of CH_3OCH_3), basic sites (formation of CO/CO_2), and redox sites (formation of HCHO and CH_3OOCH). The supported WO_3 catalysts exclusively yielded CH_3OCH_3 as the reaction product during CH_3OH-TPSR demonstrating their surface acidic nature. The CH_3OH-TPSR spectra also allowed determination of the number of surface acid sites (reflected in the area underneath the DME curve) and the kinetics or strength of the surface acid sites (reflected by the Tp value). Furthermore, using the Redhead equation it was possible to directly determine the activation energy for the surface reaction (E_{act}) in dimethyl ether formation and the kinetics for the rate-determining step (k_{rds}), which involves the first-order C–O bond scission of the surface methoxy (CH_3O^*) intermediate [31].

3.5.1. *Supported WO_3/Al_2O_3 catalysts*

The DME/CH_3OH-TPSR spectra from the supported WO_3/Al_2O_3 catalysts are shown in Fig. 8 and the Tp values are listed in Table 2. The DME/CH_3OH-TPSR spectra exhibit increasing Tp values with increasing tungsten oxide surface density. The supported surface WO_x monolayer on alumina exhibits a Tp value of 206 °C compared with 196 °C for the WO_3-free Al_2O_3 support and 254 °C for bulk WO_3. The absence of a DME-TPSR peak at 196 °C reveals that exposed alumina supports sites are not present at monolayer surface WO_x coverage. Increasing the tungsten oxide surface density above monolayer coverage further increases the Tp temperature from 206 to 226 °C indicating that the crystalline WO_3 NPs present in this tungsten oxide surface density region are less active than the surface WO_x monolayer on Al_2O_3 for the acid catalyzed methanol dehydration reaction. Thus, the surface WO_x monolayer on Al_2O_3 is more reactive than WO_3 NPs and bulk WO_3. In addition to these reactivity changes with tungsten oxide surface density, the number of catalytic active sites monotonically decreases above monolayer tungsten oxide surface coverage with increasing W/nm^2 reflecting the presence of less dispersed crystalline WO_3 NPs.

Table 2
DME/CH_3OH-TPSR Tp temperature (°C) for the supported WO_3 catalysts on the model oxide supports (TiO_2, Nb_2O_5, Al_2O_3, and ZrO_2)

Sample (calcination temperature, °C)	Surface density (W/nm^2)	DME peak temperature (°C)
Bulk TiO_2	0.0	325
7.3 wt% WTi (450)	4.0	289
8.1 wt% WTi (450)	4.5	289
13.6 wt% WTi (450)	8.0	264
16.4 wt% WTi (450)	10.0	260
19.1 wt% WTi (450)	12.0	259
Bulk Nb_2O_5	0.0	300
9.2 wt% WNb (450)	4.0	286
10.2 wt% WNb (450)	4.5	286
16.9 wt% WNb (450)	8.0	277
20.3 wt% WNb (450)	10.0	272
23.4 wt% WNb (450)	12.0	271
Bulk Al_2O_3		196
21.5 wt% WAl (450)	4.0	204
23.5 wt% WAl (450)	4.5	206
25.6 wt% WAl (450)	5.0	208
29.1 wt% WAl (450)	6.0	219
35.4 wt% WAl (450)	8.0	223
40.7 wt% WAl (450)	10.0	225
45.1 wt% WAl (450)	12.0	226
57.8 wt% WAl (450)	20.0	226
Bulk ZrO_2	0.0	374
3 wt% WZr (450)	1.3	327
5 wt% WZr (450)	2.3	319
6 wt% WZr (450)	2.8	305
8.3 wt% WZr (450)	4.0	297
9.4 wt% WZr (450)	4.5	290
10 wt% WZr (450)	4.8	286
15 wt% WZr (450)	7.6	268
20 wt% WZr (450)	10.8	266
25.0 wt% WZr (450)	14.4	262
40.0 wt% WZr (450)	28.9	259

3.5.2. *Supported WO_3/ZrO_2 catalysts*

The DME/CH_3OH-TPSR spectra for the supported WO_3/ZrO_2 catalysts are presented in Fig. 9 and listed in Table 2.

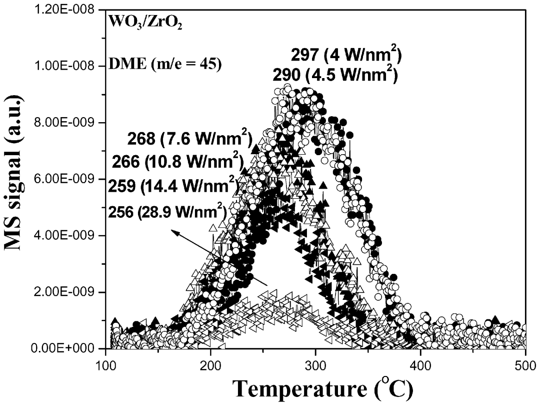

Fig. 9. CH_3OH-TPSR spectra for methanol dehydration to DME over the model supported WO_3/ZrO_2 catalysts as a function of tungsten oxide surface density (W/nm^2).

In contrast to the supported WO_3/Al_2O_3 catalyst system that exhibits an increase in DME/CH_3OH-TPSR Tp values with increasing W/nm^2, the supported WO_3/ZrO_2 catalysts exhibit a decrease in DME/CH_3OH-TPSR Tp values with increasing W/nm^2. The surface WO_x monolayer on ZrO_2 exhibits a Tp value of 290 °C that is greater than crystalline bulk WO_3 at 254 °C and less than the WO_3-free ZrO_2 support at 374 °C. At high tungsten oxide surface density, the Tp value approaches that of bulk WO_3 particles. Thus, the crystalline WO_3 NPs are more active than the surface WO_x monolayer on the ZrO_2 support and dominate the catalytic properties at high tungsten oxide surface density. Furthermore, the number of catalytic active sites decreases with increasing tungsten oxide surface density above monolayer surface coverage because of the presence crystalline WO_3 NPs above monolayer coverage.

3.5.3. *Supported WO_3/Nb_2O_5 catalysts*

The DME/CH_3OH-TPSR spectra for the supported WO_3/Nb_2O_5 catalysts follow a similar trend as that for supported WO_3/ZrO_2 and are not shown for brevity. The DME/CH_3OH-TPSR Tp values for the supported WO_3/Nb_2O_5 catalysts are listed in Table 2 and the Tp values decrease with increasing tungsten oxide surface density. The Tp value for the surface WO_x monolayer on Nb_2O_5 is 286 °C, which is higher than that for bulk WO_3 at 254 °C and less than that for the WO_3-free Nb_2O_5 support at 300 °C. Increasing the tungsten oxide surface density on Nb_2O_5 above monolayer surface WO_x coverage further decreases the Tp values from 286 to 271 °C, which reveals that the WO_3 NPs are more active than the surface WO_x species anchored to the Nb_2O_5 support. As for the supported WO_3/Al_2O_3 and WO_3/ZrO_2 catalyst systems, the number of catalytic active sites decreases with increasing tungsten oxide surface density above monolayer surface WO_x coverage on Nb_2O_5.

3.5.4. *Supported WO_3/TiO_2 catalysts*

The DME/CH_3OH-TPSR spectra for the supported WO_3/TiO_2 catalysts follow the trends found for the supported WO_3/ZrO_2 and WO_3/Nb_2O_5 catalyst systems and are not shown for brevity. The associated Tp values are listed in Table 2 and the Tp values decrease with increasing tungsten oxide surface density. The monolayer surface WO_x species on TiO_2 exhibits a Tp value of 289 °C compared with 254 °C for bulk WO_3 and 325 °C for the WO_3-free TiO_2 support. The activity of the monolayer surface WO_x monolayer on TiO_2 is comparable to that of the surface WO_x monolayer on Nb_2O_5 and ZrO_2, but at higher surface density, the supported WO_3/TiO_2 catalyst system is slightly more active than the supported WO_3/Nb_2O_5 and WO_3/ZrO_2 catalyst systems. As for the other supported WO_3 catalysts, the number of catalytic active sites decreases with increasing tungsten oxide surface density above monolayer surface WO_x coverage because of the presence of crystalline WO_3 NPs.

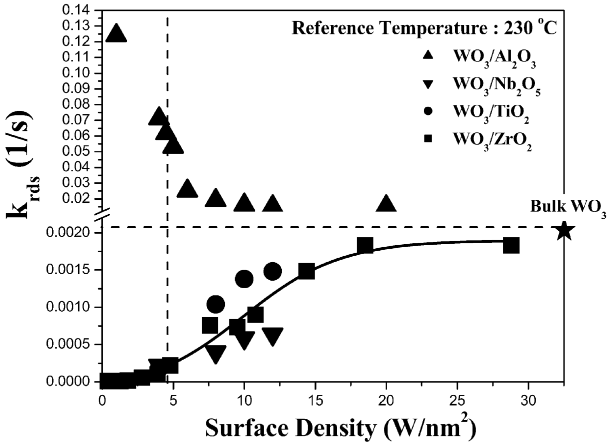

Fig. 10. First-order kinetic rate constants, k_{rds}, for CH_3OH dehydration to DME over the model-supported WO_3 catalysts as a function of tungsten oxide surface density (W/nm^2).

3.5.5. *Comparison of DME/CH_3OH-TPSR results for the supported WO_3 catalysts*

The first-order k_{rds} kinetic rate constants for methanol dehydration to dimethyl ether over the supported WO_3 catalysts at 230 °C are plotted in Fig. 10 as a function of tungsten oxide surface density. The kinetic k_{rds} values were determined from the DME/CH_3OH-TPSR Tp values and application of the Redhead equation (see Section 2.5 above for details). The supported WO_3/TiO_2, WO_3/Nb_2O_5, and WO_3/ZrO_2 catalyst systems follow the exact same k_{rds} trend, increasing as a function of W/nm^2 and approach the activity value of bulk WO_3 at high W/nm^2 values. In contrast, the supported WO_3/Al_2O_3 catalyst system follows an inverse k_{rds} trend, decreasing as a function of W/nm^2 and does not approach the value of bulk WO_3 at high W/nm^2 values. Even at the highest tungsten oxide surface density, the supported WO_3/Al_2O_3 catalysts are about an order of magnitude more active than bulk WO_3 and the other supported WO_3 catalysts. The initial high k_{rds} values for supported WO_3/Al_2O_3 below monolayer surface coverage are related to exposed alumina sites, but all of the alumina sites are covered with the surface WO_x monolayer at monolayer surface coverage and higher W/nm^2. This suggests that the surface WO_x species coordinated to the Al_2O_3 surface are highly active acid sites and even more active than the supported WO_3 NPs for methanol dehydration.

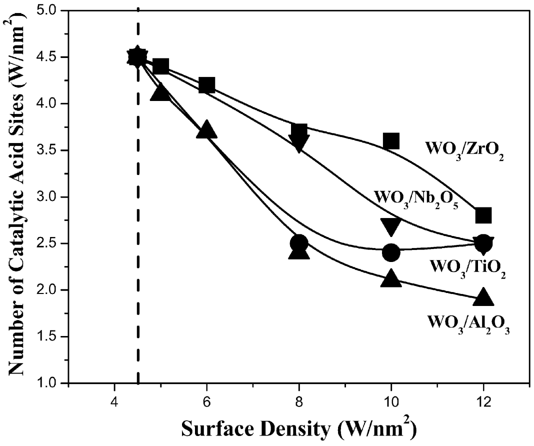

Fig. 11. Number of catalytic active sites for the model-supported WO_3 catalysts as a function of tungsten oxide surface density (W/nm^2).

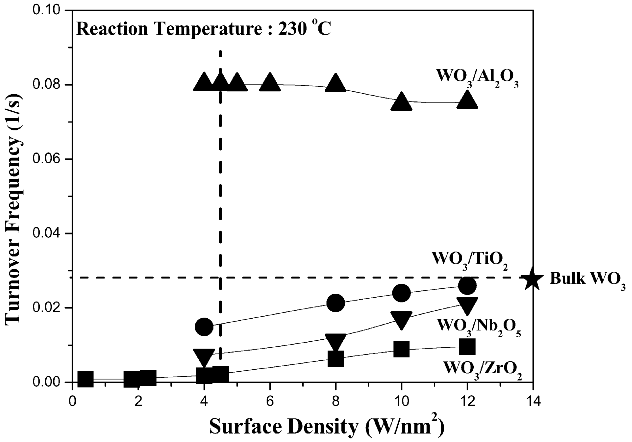

Fig. 12. Catalytic acidity TOF values for CH_3OH dehydration to DME over the model-supported WO_3 catalysts as function of tungsten oxide surface density (W/nm^2).

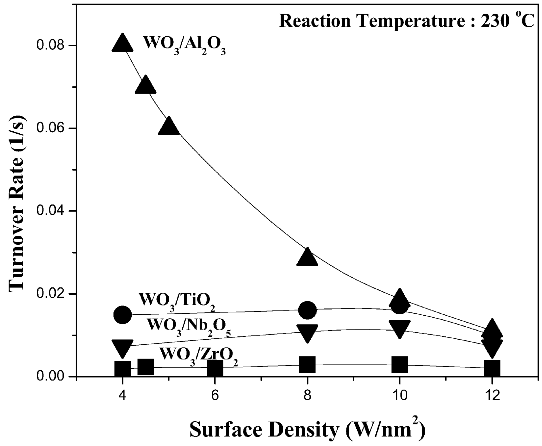

Fig. 13. Catalytic acidity TOR values for CH_3OH dehydration to DME over the model-supported WO_3 catalysts as a function of tungsten oxide surface density (W/nm^2).

The number of catalytic active sites for the supported WO_3 catalysts is plotted as a function of W/nm^2 in Fig. 11. For all supported WO_3 catalyst systems, the number of catalytic active sites decreases with W/nm^2 above monolayer coverage because of the presence of crystalline WO_3 NPs on top of the surface WO_x monolayer in this coverage region. The slight differences in the decrease in N_s with W/nm^2 for the different supported WO_3 catalyst systems may be related to the different surface areas and pore structures of the oxide supports.

3.6. Steady-state methanol dehydration kinetics

The turnover frequency (TOF) values (methanol molecules dehydrated per exposed tungsten oxide site per second) for the supported WO_3 catalysts at 230 °C are presented in Fig. 12 as a function of the W/nm^2. The TOF values were determined from knowledge of the number of catalytic active sites obtained from the CH_3OH-TPSR spectra shown in Fig. 11. The relative TOF values of the surface acidic catalytic active sites at monolayer surface WO_x coverage follow the trend $WO_3/Al_2O_3 \gg$ bulk $WO_3 > WO_3/TiO_2 > WO_3/Nb_2O_5 > WO_3/ZrO_2$. The presence of WO_3 NPs above monolayer surface coverage further alters the TOF values. For the supported WO_3/Al_2O_3 catalyst system, the TOF value decreases above monolayer surface coverage because of the lower activity of the WO_3 NPs relative to the surface WO_x sites anchored to the alumina support. For the supported WO_3/TiO_2, WO_3/Nb_2O_5, and WO_3/ZrO_2 catalyst systems, the TOF increases above monolayer surface coverage because of the higher activity of the WO_3 NPs compared with the surface WO_x species coordinated to these oxide supports. The TOF values of the nonalumina-supported tungsten oxide catalysts asymptotically approach the TOF value of bulk WO_3 at very high W/nm^2 values. The TOF value of the supported WO_3/Al_2O_3 catalyst system, however, remains much higher than the TOF for bulk WO_3 at high W/nm^2. The different trends reflect the contributions of the surface WO_x monolayer relative to WO_3 NPs toward methanol dehydration.

The turnover rates (TOR), number of methanol molecules dehydrated per all W oxide atoms in the catalyst per second, of the supported WO_3 catalysts as a function of W/nm^2 at 230 °C are presented in Fig. 13. For the submonolayer region, the TOF and TOR values are identical because the supported tungsten oxide is 100% dispersed on the supports. Above monolayer surface coverage, TOF is always greater than TOR because the supported tungsten oxide phase is not 100% dispersed on the supports. The poorly dispersed crystalline WO_3 NPs are also present above monolayer surface coverage and decrease the TOR values because all of the W oxide atoms are used in normalizing the reaction rate. The maximum TOR values for the supported WO_3 catalysts, with the exception of supported WO_3/Al_2O_3, occurs at ∼8–10 W/nm^2. At higher W/nm^2 values (>10 W/nm^2), the TOR values for all of the supported WO_3 catalyst systems asymptotically approach the same value. The similar TOR value at high W/nm^2 is a consequence of the predominance of the bulk-like WO_3 crystallites and their associated low dispersion at these high tungsten oxide surface density values.

A more detailed comparison of TOR and TOF values is shown for the supported WO_3/ZrO_2 catalyst system in Fig. 14 (note that the y-scales are different for TOR and TOF). The

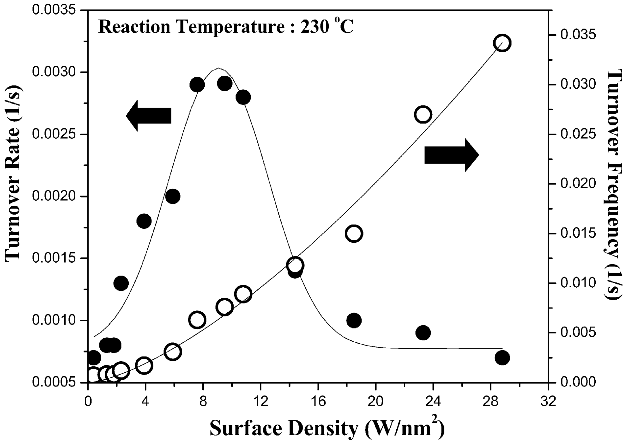

Fig. 14. Comparison of catalytic acidity TOR and TOF values for the model-supported WO_3/ZrO_2 catalysts as a function of tungsten oxide surface density (W/nm^2).

TOF and TOR values increase continuously with increasing W/nm^2 below monolayer coverage. The similar TOF and TOR trend is related to the 100% dispersion of the supported tungsten oxide phase in the submonolayer region. The increasing TOF and TOR values with surface tungsten oxide density (W/nm^2) below monolayer coverage reflect the greater catalytic acidity of the surface polytungstate species compared with the surface monotungstate species. The further increase in TOF and TOR values between 5 and 10 W/nm^2 demonstrates that the WO_3 NPs are more active than the surface WO_x species. Above 10 W/nm^2, the low dispersion of the bulk-like WO_3 particles significantly decreases the TOR values as the TOF values continue to increase. The continued increase of the TOF catalytic acidity values reflects the higher specific catalytic acidity of the bulk-like WO_3 particles relative to the WO_3 NPs.

4. Discussion

4.1. Tungsten oxide monolayer surface coverage

The Raman spectra of the supported WO_3 catalysts quantitatively demonstrate that tungsten oxide monolayer surface coverage on the model oxide supports corresponds to ~4.5 W/nm^2. Below ~4.5 W/nm^2, surface WO_x species predominate, and only minor amounts of crystalline WO_3 NPs are present as monolayer surface coverage is approached (see Figs. 1–5). From corresponding X-ray photoelectron spectroscopy (XPS) surface analysis of the surface W/Zr ratio as a function of W/nm^2 for the same model-supported WO_3/ZrO_2 catalysts, monolayer surface coverage was determined to occur at ~4.8 W/nm^2 [35]. The conclusion that the tungsten oxide monolayer surface coverage on model oxide supports corresponds to ~4.5–4.8 W/nm^2 is in agreement with almost all previous monolayer surface coverage determinations that for model-supported WO_3 catalysts monolayer coverage corresponds to ~4–5 W/nm^2 and is independent of the specific oxide support with the exception of the weakly interacting supported WO_3/SiO_2 catalyst system [15,17,21,24,25,36–50].

4.2. Molecular and electronic structures of the supported tungsten oxide phases

All of the supported WO_3 catalysts exhibit Raman bands for the dehydrated surface WO_x species between ~1000 and 1020 cm^{-1} as the tungsten oxide surface density is increased in the submonolayer coverage region (see Figs. 1–4). The corresponding UV–vis DRS Eg values for supported WO_3/Al_2O_3 and WO_3/ZrO_2 catalyst systems decrease simultaneously with increasing tungsten oxide surface density, reflecting an increase in extent of polymerization of the surface WO_x species with increasing surface coverage (see Fig. 6). The simultaneous increase in the Raman vibrational band position of the terminal W=O bond and the decrease in UV–vis DRS Eg values for the supported WO_3/Al_2O_3 and WO_3/ZrO_2 catalyst systems reflect the polymerization of the surface WO_x species with surface coverage on these model oxide supports. Although the UV–vis DRS Eg values cannot be obtained for the supported WO_3/TiO_2 and WO_3/Nb_2O_5 catalyst systems, the Raman shift from ~1000 to 1016 cm^{-1} also reflects the polymerization of the surface WO_x species on these model oxide supports, especially supported WO_3/TiO_2, with increasing tungsten oxide surface density. Consequently, the surface WO_x species progressively polymerize with increasing tungsten oxide surface density in the submonolayer region on these model oxide supports.

Above monolayer surface coverage of the 2D surface WO_x phase, 3D crystalline WO_3 NPs are present between ~5 and ~10 W/nm^2. Raman readily detects the crystalline WO_3 phase because of the significantly stronger Raman cross-section of bulk WO_3 crystals than the surface WO_x species [34]. The HR-TEM images reveal that the supported crystalline WO_3 particles on ZrO_2 are on the order of ~1 nm in size between 5 and 12 W/nm^2. The NP dimension of the supported crystalline WO_3 phase is also reflected in both its broader Raman bands and higher Eg values relative to large bulk WO_3 crystals. At very high tungsten oxide surface density, the crystalline WO_3 NPs are larger and begin to reflect the electronic structural characteristic of large bulk crystalline WO_3 particles.

4.3. Number of exposed surface catalytic active acid sites

The number of surface acid sites was quantitatively determined from the amount of DME formed during the CH_3OH-TPSR experiment (see Fig. 11). Below tungsten oxide monolayer surface coverage (<5 W/nm^2), the number of surface acid sites increases *linearly* with the tungsten oxide surface density. Above monolayer surface coverage, the number of exposed surface acid sites continuously *decreases* with tungsten oxide surface density on all of the supports because of the presence of crystalline WO_3 NPs. The crystalline WO_3 NPs reside on top of the surface WO_x monolayer and also cover up some of the surface WO_x acid sites. The trend in the quantitative decrease in the number of surface acid sites varies only slightly with tungsten oxide surface density among the different oxide supports. Furthermore, above tungsten oxide monolayer surface coverage, the surface acid sites are associated with both the surface WO_x species and the WO_3 NPs.

4.4. Relative catalytic acidity of surface WO_x species and crystalline WO_3

The relative catalytic acidity of the surface monotungstate and polytungstate WO_x species and the WO_3 NPs is dependent on the specific oxide support and was determined by the kinetics of DME formation during CH_3OH-TPSR (see Fig. 10). For all of the supports investigated, the surface polytungstate WO_x species are more acidic than the surface monotungstate WO_x species. This is reflected in the higher catalytic acid activity of the monolayer surface coverage catalysts with the corresponding submonolayer surface coverage catalysts. The catalytic acid activity of the submonolayer-supported WO_3/Al_2O_3 catalyst could not be determined because the exposed surface Al sites were very active and overwhelmed the surface reactivity of the surface monotungstate WO_x species at low surface coverage.

For the supported WO_3/Al_2O_3 catalytic system, the surface WO_x species at monolayer coverage are more acidic than the WO_3 NPs. The supported WO_3 NPs are more acidic than the surface WO_x species for the supported WO_3/Nb_2O_5, WO_3/TiO_2, and WO_3/ZrO_2 catalytic systems, however. This reveals the important contribution of the specific oxide support to the acidic character of the surface WO_x species. The catalytic acidity at tungsten oxide monolayer surface coverage increases with increasing support cation electronegativity (cation electronegativity, $Zr < Nb \sim Ti < Al$) [51]. The greater the support cation electronegativity, the less electron density resides on the bridging W–O–support bond (less basic and more acidic). This reflects the ability of the support cation to tune the acidic character of the surface WO_x species relative to the WO_3 NPs. With the exception of the supported WO_3/Al_2O_3 catalytic system, which has an extremely acidic surface WO_x monolayer, the large WO_3 particles present on Nb_2O_5, TiO_2, and ZrO_2 are more acidic than the surface WO_x species and the WO_3 NPs.

4.5. Steady-state TOF catalytic acidity values

For the supported WO_3/Al_2O_3 catalyst system, the TOF catalytic acidity values slightly decreased above tungsten oxide monolayer surface coverage because of the less acidic WO_3 NPs relative to the surface WO_x monolayer ($TOF_{\text{Polytungstate}} > TOF_{WO_3,\text{NPs}}$). However, the TOF catalytic acidity values increased continuously with tungsten oxide surface density for supported WO_3/Nb_2O_5, WO_3/TiO_2, and WO_3/ZrO_2, indicating that $TOF_{\text{Monotungstate}} < TOF_{\text{Polytungstate}} < WO_{3,\text{NPs}} < WO_{3,\text{Bulk}}$. Thus, the overall TOF catalytic acidity depends on the intrinsic catalytic acidity of the surface WO_x species and the WO_3 NPs, as well as on their relative contributions to the total number of exposed surface acid sites. Consequently, there is no standard relationship between the tungsten oxide domain size and the specific catalytic acidity because of the significant role of the specific oxide support ligand on the acidity of the surface WO_x species.

4.6. Steady-state TOR catalytic acidity values

The steady-state TOR catalytic acidity values are sometimes also reported in the catalysis literature because the actual number of exposed surface tungsten oxide sites is not determined. As a result, the reaction rate data are normalized by all of the atoms present in the supported metal oxide phase, all of the W oxide atoms in supported WO_3 catalysts. Consequently, the actual dispersion of the supported WO_3 phase is not taken into consideration. The current study with the model-supported WO_3 catalysts allows a direct comparison between steady-state TOF and TOR values for the same catalysts and reaction where the dispersion of the supported WO_3 phase is known. The steady-state TOR and TOF catalytic acidity values for CH_3OH dehydration are identical in the submonolayer region and at monolayer surface coverage because the supported WO_3 phase is 100% dispersed as surface WO_x species on the oxide support. Above tungsten oxide monolayer surface coverage, the TOR and TOF catalytic acidity values begin to deviate because the presence of 3D crystalline WO_3 NPs decreases the supported WO_3 dispersion. As a result, the TOF catalytic acidity values will always be greater than the corresponding TOR catalytic acidity values because TOR overcounts the number of actual exposed catalytic acid sites above monolayer surface coverage. This overcounting of exposed catalytic active sites in the determination of TOR results in decreasing the TOR catalytic acidity values at high tungsten oxide surface density.

For the supported WO_3/Al_2O_3 catalysts above monolayer coverage, the TOR catalytic acidity values decrease with increasing W/nm^2 because of the overcounting of the exposed surface sites and the lower intrinsic catalytic acidity of the WO_3 NPs (see Fig. 13). As mentioned earlier, the TOR catalytic acidity values for the supported WO_x species on Al_2O_3 cannot be determined below monolayer coverage because of the much greater catalytic acidity of the exposed surface Al sites in the submonolayer region.

For the other supported WO_3 model catalysts (supported WO_3/Nb_2O_5, WO_3/TiO_2, and WO_3/ZrO_2), the TOR catalytic acidity values increase between ∼5 and 10 W/nm^2 because of the much higher intrinsic catalytic acidity of the WO_3 NPs relative to the surface WO_x species (see Figs. 13 and 14), while the number of actual catalytic active sites decreases by only less than a factor of 2 (see Fig. 12). For tungsten oxide surface density $> 10\ W/nm^2$, the decrease in the number of actual catalytic acid sites is greater than the modest increase in catalytic acidity from the bulk-like WO_3 particles and, thus, results in an overall decrease in TOR catalytic acidity values. Consequently, the initial increase and subsequent decrease of the TOR catalytic acidity values with W/nm^2 above monolayer coverage is just a consequence of (i) the relative intrinsic catalytic activity of the WO_3 NPs and the surface WO_x monolayer, (ii) the partition of exposed catalytic acidic sites between the WO_3 NPs and the surface WO_x species, and (iii) ratio of actual number of exposed catalytic acid sites and the total number of W oxide atoms in the supported tungsten oxide phase. Thus, the maximum in the TOR catalytic acidity values with W/nm^2 for model-supported WO_3/ZrO_2, WO_3/Nb_2O_5, and WO_3/TiO_2 catalysts is primarily a consequence of overcounting the actual number of catalytic acidic sites present in supported WO_3 catalysts at high W/nm^2 values.

5. Conclusion

The nature of the dehydrated surface tungsten oxide phase is found to be the same on the different supports examined (Al_2O_3, ZrO_2, TiO_2, and Nb_2O_5) as a function of W/nm^2. In the submonolayer region ($<5\ W/nm^2$), both monotungstate and polytungstate surface WO_x species are present, and the ratio of polytungstate/monotungstate increases with tungsten oxide surface coverage. Above monolayer coverage ($>5\ W/nm^2$), 3D crystalline WO_3 NPs are present on top of the 2D surface WO_x monolayer. Above $\sim 10\ W/nm^2$, bulk-like WO_3 large particles are also present. These different molecular structures of the supported tungsten oxide phase affect the overall dispersion of the supported WO_3 catalysts. The dispersion is 100% in the submonolayer region and decreases continuously with increasing tungsten oxide loading above monolayer coverage due to the presence of the crystalline WO_3 particles.

The relative catalytic acidity of the different tungsten oxide components depends on the specific oxide support. For supported WO_3/Al_2O_3 catalysts, the surface WO_x species are more active than the crystalline WO_3 particles. For the other supported WO_3 catalysts, however, the crystalline WO_3 particles are more active than the surface WO_x species. These different catalytic acidity patterns of the different tungsten oxide structures reflect the important effect of the specific oxide support on the relative acidic activity of the surface WO_x species to the WO_3 NPs. As the support cation electronegativity increases (Al $>$ Nb $\sim$ Ti $>$ Zr), the electron density of the bridging W–O–support bond deceases and results in a more acidic site. Consequently, there is no general relationship between the tungsten oxide structure/domain size and the specific catalytic acidity.

Acknowledgment

Support from the U.S. Department of Energy, Division of Basic Energy Sciences (Grant DE-FG 02-93 ER 14350) is gratefully acknowledged.

References

[1] C.L. Thomas, Catalytic Processes and Proven Catalysts, Academic Press, New York, 1970.
[2] C.N. Satterfield, Heterogeneous Catalysis in Practice, McGraw–Hill, New York, 1980.
[3] L.L. Murrell, C.J. Kim, D.C. Grenoble, US Patent 4 233 139 (1980).
[4] D.C. Grenoble, C.J. Kim, L.L. Murrell, US Patent 4 440 872 (1984).
[5] J. Bernholc, J.A. Horsley, L.L. Murrell, L.G. Sherman, S. Soled, J. Phys. Chem. 91 (1987) 1526.
[6] L.L. Murrell, D.C. Grenoble, C.J. Kim, N.C. Dispenziere, J. Catal. 107 (1987) 463.
[7] C. Wivel, B.S. Clausen, R. Candia, S. Morup, H. Topsoe, J. Catal. 87 (1984) 497.
[8] I.E. Wachs, C.C. Chersich, J. Hardenbergh, Appl. Catal. 13 (1985) 335.
[9] M. Ai, J. Catal. 49 (1977) 305.
[10] S. Morikawa, K. Takahashi, J. Mogi, S. Kurita, Bull. Chem. Soc. Jpn. 55 (1982) 2254.
[11] M. Hino, K. Arata, J. Chem. Soc. Chem. Commun. 18 (1988) 1259.
[12] J.G. Santiesteban, J.C. Vartuli, S. Han, R.D. Bastian, C.D. Chang, J. Catal. 168 (1997) 431.
[13] M. Hino, K. Arata, Chem. Lett. 6 (1989) 971.
[14] C. Martin, G. Solana, P. Malet, V. Rives, Catal. Today 78 (2003) 365.
[15] D.S. Kim, M. Ostromecki, I.E. Wachs, J. Mol. Catal. A Chem. 106 (1996) 93.
[16] J.-M. Jehng, A.M. Turek, I.E. Wachs, Appl. Catal. A 83 (1992) 179.
[17] I.E. Wachs, Catal. Today 27 (1996) 437.
[18] R. Thomas, F.P.J.M. Kerkhof, J.A. Moulijn, J. Medema, V.H.J. de Beer, J. Catal. 61 (1980) 559.
[19] P. Tiltarelli, A. Iannibello, P. Villa, J. Solid State Chem. 37 (1981) 95.
[20] S.S. Chan, I.E. Wachs, L.L. Murrell, L. Wang, W.K. Hall, J. Phys. Chem. 88 (1984) 5831.
[21] L. Salvati, L.E. Makovsky, J.M. Stencel, F.R. Brown, D.M. Hercules, J. Phys. Chem. 85 (1981) 3700.
[22] P. Biloen, G. Pott, J. Catal. 30 (1973) 169.
[23] S. Djerad, L. Tifouti, M. Crocoll, W. Weisweiler, J. Mol. Catal. A Chem. 208 (2004) 257.
[24] J.A. Horsley, I.E. Wachs, J.M. Brown, G.H. Via, F.D. Hardcastle, J. Phys. Chem. 91 (1987) 4014.
[25] M.M. Ostromecki, L.J. Burcham, I.E. Wachs, J. Mol. Catal. A Chem. 132 (1998) 59.
[26] L.H. Gielgens, M.G.H. Vankampen, M.M. Broek, R. Vanhardeveld, V. Ponec, J. Catal. 154 (1995) 201.
[27] J. Macht, C.D. Baertsch, M.M. Lozano, S.L. Soled, Y. Wang, E. Iglesia, J. Catal. 227 (2004) 479.
[28] T. Feng, J.M. Vohs, J. Catal. 208 (2002) 301.
[29] L.E. Briand, W.E. Farneth, I.E. Wachs, Catal. Today 62 (2000) 219.
[30] P.A. Redhead, Vacuum 12 (1962) 213.
[31] E.I. Ross, T.J. Kim, I.E. Wachs, in preparation.
[32] L.A. Nafie, in: I.R. Lewis, H.G.M. Edwards (Eds.), Handbook of Raman Spectroscopy, Dekker, New York, 2001, p. 1.
[33] M.A. Vuurman, I.E. Wachs, J. Phys. Chem. 96 (1992) 5008.
[34] S.S. Chan, I.E. Wachs, L.L. Murrell, J. Catal. 90 (1984) 150.
[35] W.V. Knowles, Ph.D. dissertation, Rice University, Houston, TX (2006).
[36] M. Scheithauer, R.K. Grasselli, H. Knozinger, Langmuir 14 (1998) 3019.
[37] Y.S. Chen, I.E. Wachs, J. Catal. 217 (2003) 468.
[38] M. Scheithauer, T.K. Cheung, R.E. Jentoft, R.K. Grasselli, B.C. Gates, H. Knozinger, J. Catal. 180 (1998) 1.
[39] C.D. Baertsch, S.L. Soled, E. Iglesia, J. Phys. Chem. B 105 (2001) 1320.
[40] D.G. Barton, M. Shtein, R.D. Wilson, S.L. Soled, E. Iglesia, J. Phys. Chem. B 103 (1999) 630.
[41] N. Vaidyanathan, M. Houalla, D.M. Hercules, Catal. Lett. 43 (1997) 209.
[42] N. Vaidyanathan, D.M. Hercules, M. Houalla, Anal. Bioanal. Chem. 373 (2002) 547.
[43] N. Vaidyanathan, M. Houalla, D.M. Hercules, Surf. Interface Anal. 26 (1998) 415.
[44] C. Pfaff, M.J. Perez-Zurita, C. Scott, P. Patino, M.R. Goldwasser, J. Goldwasser, F.M. Mulcahy, M. Houalla, D.M. Hercules, Catal. Lett. 49 (1997) 13.
[45] N. Naito, N. Katada, M. Niwa, J. Phys. Chem. B 103 (1999) 7206.
[46] X.F. Yu, N.Z. Wu, H.Z. Huang, Y.C. Xie, Y.Q. Tang, J. Mater. Chem. 11 (2001) 3337.
[47] J. Engweiler, J. Harf, A. Baiker, J. Catal. 159 (1996) 256.
[48] G. Bond, S. Flamerz, L. van Wijk, Catal. Today 1 (1987) 229.
[49] S.S. Chan, I.E. Wachs, L.L. Murrell, N.C. Dispenziere Jr., J. Catal. 92 (1985) 1.
[50] L. Salvati, J.M. Makovsky, J.M. Stencel, F.R. Brown, D.M. Hercules, J. Phys. Chem. 85 (1981) 3700.
[51] R.T. Sanderson, J. Chem. Educ. 65 (1988) 112.